Publication Year	2024
Acceptance in OA	2025-01-21T11:30:11Z
Title	The curious case of 2MASS J15594729+4403595, an ultra-fast M2 dwarf with possible Rieger cycles
Authors	MESSINA, Sergio, CATANZARO, Giovanni, LANZA, Antonino Francesco, Gandolfi, D., Serrano, M. M., Deeg, H. J., García-Alvarez, D.
Publisher's version (DOI)	10.1051/0004-6361/202449959
Handle	http://hdl.handle.net/20.500.12386/35674
Journal	ASTRONOMY & ASTROPHYSICS
Volume	691

A&A, 691, A117 (2024)
https://doi.org/10.1051/0004-6361/202449959

Astronomy & Astrophysics

The curious case of 2MASS J15594729+4403595, an ultra-fast M2 dwarf with possible Rieger cycles

S. Messina[1,⋆], G. Catanzaro[1], A. F. Lanza[1], D. Gandolfi[3], M. M. Serrano[2],
H. J. Deeg[4], and D. García-Alvarez[4]

[1] INAF-Catania Astrophysical Observatory, Via S. Sofia, 78, I-95127 Catania, Italy
[2] Mizar Observatory, Madrid, Spain
[3] Dipartimento di Fisica, Universitá degli Studi di Torino, Via Pietro Giuria 1, I-10125 Torino, Italy
[4] Instituto de Astrofisica de Canarias, 38205 La Laguna, Tenerife, Spain

Received 13 March 2024 / Accepted 14 August 2024

ABSTRACT

Context. RACE-OC (Rotation and ACtivity Evolution in Open Clusters) is a project aimed at characterising the rotational and magnetic activity properties of the late-type members of open clusters, stellar associations, and moving groups of different ages. The evolution in time of rotation and activity at different masses sheds light on the evolution of the stellar internal structure, on magnetohydrodynamic processes operating in the stellar interior, and on the coupling and decoupling mechanisms between the radiative core and the external convective envelope. As part of this project, in the present paper we present the results of an investigation of a likely member of the AB Doradus association, the M-type star 2MASS J15594729+4403595.

Aims. In the present study, we aim to reveal the real nature of our target, which turned out to be a hierarchical triple system, to derive the stellar rotation period and surface differential rotation, and to characterise its photospheric magnetic activity.

Methods. We have collected radial velocity and photometric time series, complemented with archive data, to determine the orbital parameters and the rotation period and we have used the spot modelling technique to explore what causes its photometric variability.

Results. We found 2MASS J15594729+4403595 to be a hierarchical triple system consisting of a dwarf, SB1 M2, and a companion, M8. The M2 star has a rotation period of $P = 0.37$ d, making it the fastest among M-type members of AB Dor. The most relevant result is the detection of a periodic variation in the spotted area on opposite stellar hemispheres, which resembles a sort of Rossby wave or Rieger-like cycles on an extremely short timescale. Another interesting result is the occurrence of a highly significant photometric periodicity, $P = 0.443$ d, which may be related to the stellar rotation in terms of either a Rossby wave or surface differential rotation.

Conclusions. 2MASS J15594729+4403595 may be the prototype of a new class of extremely fast rotating stars exibiting short Rieger-like cycles. We shall further explore what may drive these short-duration cycles and we shall also search for similar stars to allow for a statistical analysis.

Key words. stars: activity – stars: late-type – stars: individual: 2MASS J15594729+4403595 – stars: rotation – starspots – open clusters and associations: general

1. Introduction

Stellar rotation is a time-dependent quantity that evolves on different timescales during the star's life. In the first stage of life, the evolution of the surface rotation is controlled by the accretion disc through a magnetic locking mechanism (Koenigl 1991; Shu et al. 1994). Once the disc is dispersed and the star is free to spin up toward the zero-age main sequence (ZAMS) owing to radius contraction, we deal with a distribution of initial rotation periods for each mass value (Gallet & Bouvier 2013; Messina 2019). It is only during the main sequence (MS) evolution that the magnetised winds will establish a one-to-one correspondence between mass and rotation period (Matt et al. 2015). Such an univocal mass-period relation is first reached by more massive stars (late-F, early-G) and by a few hundred million years it also extends to late-K and early-M stars. The evolution from ZAMS is the time range in which the gyrochronological method for the age dating of low-mass stars is applied more accurately (Barnes 2007; Silva-Beyer et al. 2022).

However, close binaries significantly deviate from this scenario, their surface rotational evolution being influenced by earlier disc dispersal and by the tidal forces between the components. A study by Messina (2019) shows that such tides are effective in altering the rotational evolution with respect to single stars, when the components are as close as about 100 au. These stars play as contaminants of the period-colour distribution and bias the average rotation towards shorter periods, which also means towards younger ages. In this respect, it is particularly challenging to unveil the real nature of very fast rotating stars, which can be either single stars in the convective sequence and migrating towards the interface sequence (Barnes 2003) or close binaries whose rotational evolution has followed a different path. It is mandatory to identify all close binaries in an open cluster, association, or moving group and remove them when the colour-period distribution has to be fitted for dating purposes (see, e.g. Messina et al. 2017a,b).

As part of the RACE-OC project (Messina et al. 2010, 2011), we focussed our attention on those members of young open clusters and associations still missing either a spectroscopic or a rotational characterisation. That was the case for

---

[⋆] Corresponding author; `sergio.messina@inaf.it`

2MASS J15594729+4403595, an M-type likely member of the AB Dor association. To measure the rotation period and characterise its possible single or binary nature, we planned a dedicated photometric and spectroscopic monitoring. Our investigation has revealed this star to be particularly interesting owing to its variable behaviour that has never been observed before and that is puzzling in a sense. A summary of literature information is presented in Sect. 2, our data and literature data in Sect. 3, periodogram and spectroscopic analyses in Sects. 4 and 5, the spot modelling results in Sect. 6, and a discussion and our conclusions in Sects. 7 and 8.

2. 2MASS J15594729+4403595

2MASS J15594729+4403595 (RA = 15:59:47.29; Dec = +44:03:59.5 (J2000); V = 11.86 mag) is an M2 + M8 visual binary system (Lépine et al. 2013; Janson et al. 2012). The M8 component was discovered by Janson et al. (2012) at an angular distance, $\rho = 5.638 \pm 0.004''$, and PA = 284.8 ± 0.3 (epoch 2009.42) from the primary M2 star. Bowler et al. (2015) confirmed the brown dwarf nature of the secondary M8 component by using near-infrared spectroscopy, inferred a mass of about $43 \pm 9\,M_J$, and put a limit on the age in the 50−200 Myr range. The physical association between the two components is inferred by the common proper motion, $\mu = 72.7$ mas yr^{-1}, reported in the NOMAD catalogue (Zacharias et al. 2005) and confirmed by Janson et al. (2012), $\mu = 73$ mas yr^{-1}. The AstraLux survey carried out by Janson et al. (2012) allowed the measurement of Sloan magnitude differences of $\Delta z' = 5.51$ mag and $\Delta i' = 6.33$ mag between the two components and the following physical parameters to be derived for the primary, A, and secondary, B, components: Sp.T$_\mathrm{A}$ = M1.0 and Sp.T$_\mathrm{B}$ = M8.0, and $M_\mathrm{A} = 0.54\,\mathrm{M}_\odot$ and $M_\mathrm{B} = 0.10\,\mathrm{M}_\odot$; a separation of 197.3 AU, derived from a spectroscopic distance of 35 pc (±37%), which turned out to be underestimated on the basis of the most recent *Gaia* measurements. The latter put this target at a larger distance of $d = 42.1 \pm 0.3$ pc and provide a re-normalised unit weight error (RUWE) for the primary component of 13.9, indicating that it is probably an unresolved binary. Zickgraf et al. (2003) identified 2MASS J15594729+4403595 as the optical counterpart of the ROSAT X-ray source 1RXS J155947.5+440358 listed in the RASS-BSC (Voges et al. 1999) with $\mathrm{Log}(L_\mathrm{X}/L_\mathrm{bol}) = -3.21$. A measure of H$\alpha$ EW = 3.3 Å was provided by Riaz et al. (2006) as part of their survey of M dwarfs in the solar neighbourhood.

3. Observations

To investigate the nature of 2MASS J15594729+4403595, we carried out photometric and spectroscopic observations and availed ourselves of the observational data that time by time were made available in public archives.

3.1. Photometry

Our own photometric observations were gathered at the Zeta UMa Observatory (Spain) in 2013 (see Appendix A for details on observations and data reduction).

About seven years after our ground-based monitoring, the Transiting Exoplanet Survey Satellite (TESS) started observing 2MASS J15594729+4403595, and precisely in Sectors 25, 50, and 51.

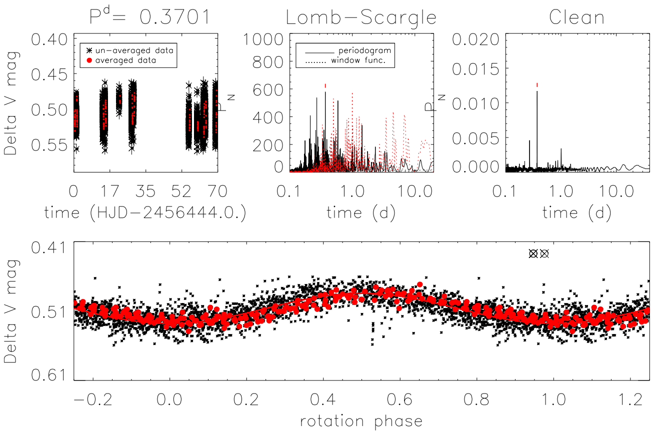

Fig. 1. Periodogram analysis of Zeta UMa Observatory V-band time series. Top: (from left to right) V magnitude time series; Lomb-Scargle periodogram; Clean periodogram. Bottom: V-band light curve phased with the 0.3701 d rotation period. The rotation phase was computed using the following ephemeris: $2456444.0990 + 0.3701 \times E$.

3.2. High-resolution spectroscopy

Eight high-resolution spectra of 2MASS J15594729+440359 were acquired in 2014, in the period between January and July, with the FIbre-fed Échelle Spectrograph FIES (Frandsen & Lindberg 1999; Telting et al. 2014) mounted on the 2.56-m Nordic Optical Telescope (NOT) of Roque de los Muchachos Observatory (La Palma, Spain), under the NOT observing programme P48-217. We used the 1.3″ medium-resolution fibre, which provides a resolving power of R = 47 800 and a wavelength coverage of about 3600–7400 Å.

Following the same observing strategy described in Gandolfi et al. (2013), in the spectroscopic reduction procedure we started removing cosmic ray hits by splitting each epoch observation into three consecutive sub-exposures and traced the radial velocity (RV) drift of the instrument by acquiring long-exposed (T_exp = 15 s) ThAr spectra right before and after each epoch observation. Data were reduced using a customised IDL software suite, which includes bias subtraction, flat-fielding, order tracing and extraction, and wavelength calibration.

4. Periodogram analysis

4.1. Zeta UMa Observatory data

We used two different periodogram analyses to search for the photometric rotation period in the photometric time series, the generalised Lomb-Scargle (GLS; Zechmeister & Kürster 2009), and the CLEAN (Roberts et al. 1987) periodograms. An estimate of the false alarm probability (FAP) was done using Monte Carlo simulations according to the approach outlined by Herbst et al. (2002). A more detailed description is given by Messina et al. (2010). The uncertainty in determining the rotation period was estimated following Lamm et al. (2004) (see also Messina et al. 2010). The results of our analysis are plotted in Figs. 1 and 2.

In the top left panel of Fig. 1, we plot the time series of the instrumental differential V magnitudes. Black asterisks and red bullets represent non-averaged and averaged observations (bin width of 15 min), respectively. In the middle panel, we plot the GLS periodogram, with the data window function (dotted red line) overplotted, along with the power corresponding to FAP = 1% (horizontal dashed line). In the right panel, we plot

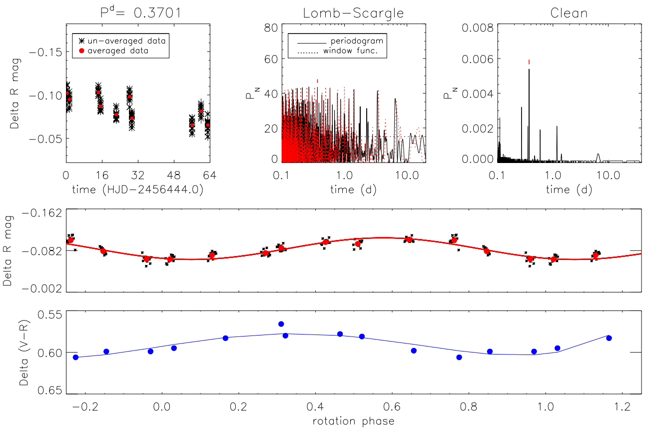

Fig. 2. Periodogram analysis of Zeta UMa Observatory *R*-band time series. Top: (from left to right) *R* magnitude time series; Lomb-Scargle periodogram; Clean periodogram. Middle: *R*-band light curve phased with the 0.3701 d rotation period. Bottom: *V*−*R* colour curve phased with the 0.3701 d rotation period.

the CLEAN power spectrum. The GLS periodogram exhibits a number of significant power peaks. The most significant peak is at $P = 0.3701 \pm 0.0005$ d, which we assume to be the stellar rotation period. We note that the same period is retrieved by the CLEAN periodogram, which exhibits less peaks owing to its capability to remove the alias arising from the data window function. In the bottom panel, we plot the light curve phased using the ephemeris $2456444.0990 + 0.3701 \times E$. The *V*-band phased light curve has an amplitude of $\Delta V = 0.04$ mag, which was obtained from the amplitude of a fitting sinusoid (solid red line) and exhibits a slight asymmetry, where the phase interval of decreasing brightness is longer than that of increasing brightness. A similar analysis was carried out with the ΔR magnitude time series. The results are plotted in Fig. 2. The *R*-band light curve has the same amplitude, $\Delta R = 0.04$ mag, but unlike the *V*-band light curve it is symmetric. The differential *V*−*R* colour curve, plotted in the bottom panel of Fig. 2, has an amplitude of $\Delta(V{-}R) = 0.03$ mag. The colour curve has its maximum around phase $\phi \simeq 0.3$, whereas the *V*- and *R*-band light curves have their maximum around phase $\phi \simeq 0.5$.

In the case of variability dominated by cool spots, we generally observe a positive correlation between the light and colour curve; when spots are most visible, and therefore the light curve has a minimum, the star is reddest, and the colour curve exhibits a minimum. In the case of variability dominated by cool and hot spots, we generally observe a negative correlation between the light and colour curves; when spots are most visible and the light curve has a minimum, the star is bluest, and the colour curve exhibits a maximum (see, e.g. Messina 2008). In the case of 2MASS J15594729+4403595, we observe during the 2013 season a sort of mixed case in which two-temperature inhomogeneities drive the observed variability; however, they are not at the same mean stellar longitudes, their photometric barycenters being separated by $\Delta\phi \simeq 0.2$, or about 70°, giving rise to the aforementioned asymmetries.

To infer the inclination of the stellar rotation axis, we combined the rotation period, stellar radius, and projected rotational velocity. The stellar radius was derived from the evolutionary track best fitting our target in the HR diagram. The 2MASS and *Gaia* magnitudes of the primary component (resolved from the M8 component in both photometries) provide colour indices in agreement with a M2 spectral type. Taking into account a slight bias towards redder wavelengths owing to the unresolved companion of the primary (SB1) component, we can assume for it a spectral type of M1.5 ± 0.5 and an effective temperature of $T_{\rm eff} = 3500 \pm 50$ K according to the Pecaut & Mamajek (2013) relations. In the HR diagram, the primary component of the SB1 system is best fit, after correction for the magnitude contribution of the unresolved unseen component, by an evolutionary track of mass $0.45 \pm 0.05\,M_\odot$ and an age in the range of 30–80 Myr (Baraffe et al. 2015). The corresponding stellar radius is $R_\odot = 0.50 \pm 0.05$. Combining the radius, rotation period, and projected rotational velocity (see Sect. 5), we derive an inclination for the stellar rotation axis of $i = 50 \pm 10°$.

4.2. TESS data

2MASS J15594729+4403595 was observed by TESS in Sectors 25, 50, and 51. In the following periodogram analyses, we used the PDCSAP fluxes extracted from the Mikulski Archive for Space Telescopes (MAST). The results of our periodogram analysis are listed in Table 1.

In each sector and in their combination, we detected three highly significant periodicities, $P_1 = 0.36996 \pm 0.00009$ d, $P_2 = 0.44298 \pm 0.0001$ d, and $P_3 = 0.18498 \pm 0.00002$ d (see Fig. 3 as an example). We first note that P_1 is in very good agreement with the period, $P = 0.3701 \pm 0.0005$ d, measured from the Zeta UMa data. Then, we note that $P_3 = P_1/2$. The more plausible explanation for the presence of P_3 is that it is the first harmonic of P_1 and it arises from the presence of spots on opposite hemispheres of the stellar surface, which are carried in and out of view with a period, P_1, and produce a double-dip modulation with minima of unequal depth, their respective areas being different. Indeed, the amplitude, A_3, of the rotational modulation associated with P_3 is about 25% of A_1. The presence of P_2 is challenging (see Sect. 7). In Fig. 4, we plot the photometric time series corresponding to the three TESS Sectors with, overplotted, the sinusoidal fit (solid red line) with all three periodicities. It is clearly visible the beating between period P_1 and P_2 which, due to their difference of approximately 15% produces a modulation of the variability amplitude with a period of about $P_1/0.15 = 2.5$ days.

5. Physical and orbital parameters

We estimated the projected rotational velocity, $v \sin i$ of 2MASS J15594729+440359, by using the spectrum of GJ 411 as a template. The spectral lines of GJ 411 are unresolved in the FIES spectra, owing to the small $v \sin i$ of the template[1]. Assuming a linear limb-darkening coefficient, $\mu = 0.65$ (for the TESS waveband centred at 786.5 nm), for early-type M-dwarf stars (Claret et al. 2012), we found that the projected rotational velocity of 2MASS J15594729+440359 is $v \sin i = 54 \pm 5$ km s^{-1}.

Radial velocity measurements were derived by performing a multi-order cross-correlation with a synthetic template computed with the atmospheric parameters typical of an M2V star and broadened for the resolving power and rotational velocity of our target. The cross-correlation was calculated paying particular attention to excluding Balmer lines from the correlation, as well as spectral intervals with telluric lines. The FIES RV measurements are listed in Table 2, along with the heliocentric Julian date (HJD) of mid-exposure, the total exposure time, and the S/N per pixel at 5500 Å.

---

[1] $v \sin i = 1.6$ km s^{-1} according to Głębocki & Gnaciński (2005).

Table 1. Results of periodogram analysis on TESS data.

TESS Sector	P_1 (d)	P_2 (d)	P_3 (d)	A_1 (mag)	A_2 (mag)	A_3 (mag)
Sector 25	0.370 ± 0.003	0.443± 0.004	0.1849 ± 0.0006	0.016	0.005	0.004
Sector 50	0.370 ± 0.003	0.443 ± 0.004	0.1849 ± 0.0006	0.015	0.006	0.003
Sector 51	0.370 ± 0.003	0.443 ± 0.004	0.1849 ± 0.0007	0.018	0.007	0.002
Sector 25–51	0.3700 ± 0.0009	0.4429 ± 0.0001	0.1850 ± 0.0002	0.016	0.006	0.0036

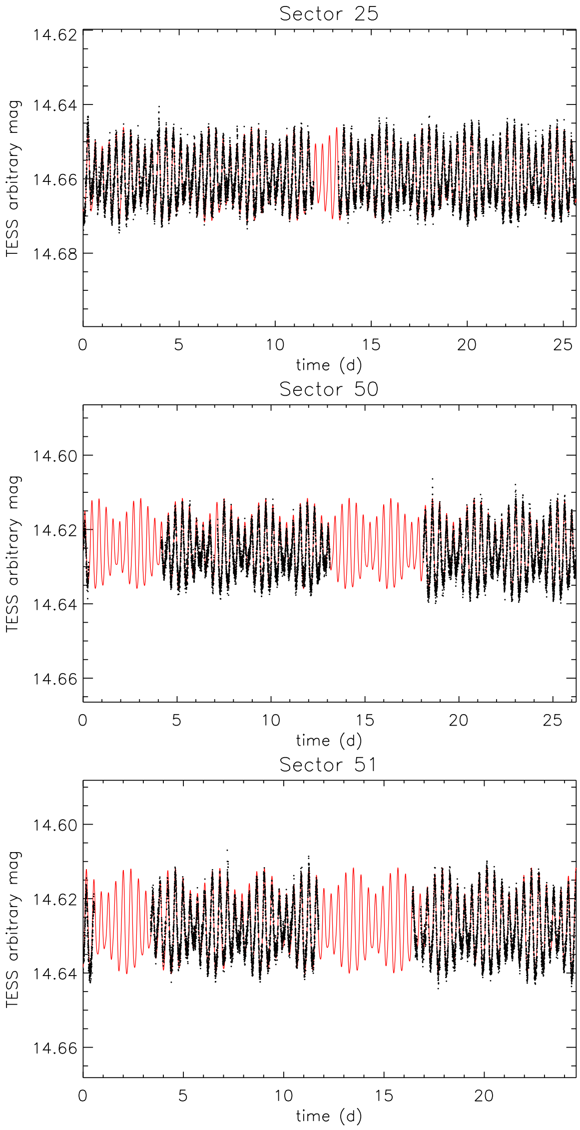

Fig. 3. TESS time series (black dots) from Sectors 25, 50, and 51 with overplotted sinusoidal fits (red line) with the three periodicities $P_1 = 0.36996$ d, $P_2 = 0.44298$ d, and $P_3 = 0.18498$ d.

The FIES spectra reveal a rapidly rotating star and strong emission in the Balmer and Ca II H and K lines, confirming the high magnetic activity level suggested by the strong X-ray luminosity. The cross-correlation function of the various epoch spectra shows an asymmetric and variable profile that we ascribe to magnetically active regions carried around by stellar rotation.

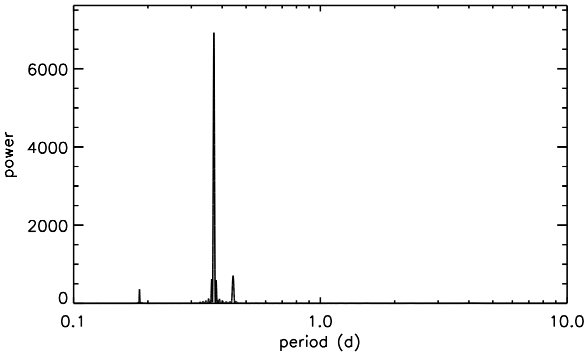

Fig. 4. Periodogram of TESS time series collected in Sect. 25. The power peaks corresponding to the three periodicities, $P_1 = 0.370$ d, $P_2 = 0.443$ d, and $P_3 = 0.18498$ d, are clearly detected. Similar periodograms are obtained when analysing Sectors 50 and 51.

As the reader can easily see in Table 2, our RV measurements are not consistent with each other. This difference may arise from orbital motion and suggests the existence of a fainter close-in companion. Therefore, the bright M2 component may be an SB1 spectroscopic binary. To investigate this hypothesis, we searched the literature for other RVs and several spectroscopic archives. The RVs of our target have been published by Malo et al. (2014), Binks & Jeffries (2016), and Jönsson et al. (2020). Moreover, we downloaded three spectra from the CFHT archive acquired in 2012, 2013, and 2014 with ESPADONS. We derived RVs for these spectra with the same procedure as we did for FIES data. In particular, the 2013 spectra is the one published by Malo et al. (2014), so we used this spectrum to check the validity of our methods. Our determination of RV is totally compatible with that published by the latter authors.

A GLS periodogram analysis (Zechmeister & Kürster 2009) of the RV time series did not reveal any significant periodicity. Therefore, in order to get a tentative orbital solution for our system, we proceeded as follows.

The RVs for a spectroscopic binary system are given by the following equation:

$$V_{\rm rad} = \gamma + K[\cos(\theta + \omega) + e\cos\omega], \tag{1}$$

where γ is the RV of the centre of mass, e is the eccentricity of the orbit, ω is the longitude of the periastron, θ is the true anomaly of the orbital motion at a given instant, and K is the semi-amplitude of the velocity curve given by the formula

$$K = \frac{2\pi a \sin i}{P\sqrt{1-e^2}}, \tag{2}$$

where P is the orbital period of the system, a its semi-major axis, and i the inclination angle.

Table 2. FIES/NOT and ESPADONS/CFHT RV measurements.

HJD	RV ($\mathrm{km\,s^{-1}}$)	σ_{RV} ($\mathrm{km\,s^{-1}}$)	T_{exp} (s)	S/N/pixel at 5500 Å
FIES/NOT				
56665.76941	−28.3	0.3	2269	31
56668.74116	−29.6	0.3	3769	49
56739.72624	−21.7	0.3	2872	60
56740.68460	−20.8	0.3	5742	70
56741.68671	−22.1	0.3	2869	55
56841.39334	−13.5	0.3	1887	60
56842.39381	−13.7	0.3	1887	50
56855.41977	−13.8	0.3	1287	40
ESPADONS/CFHT				
55970.11628	−23.5	0.5	500	30
56355.12240	−15.5	0.4	1000	30
56825.99784	−16.2	0.3	1200	30

Notes. The total exposure time and the S/N per pixel at 5500 Å are listed in the last two columns.

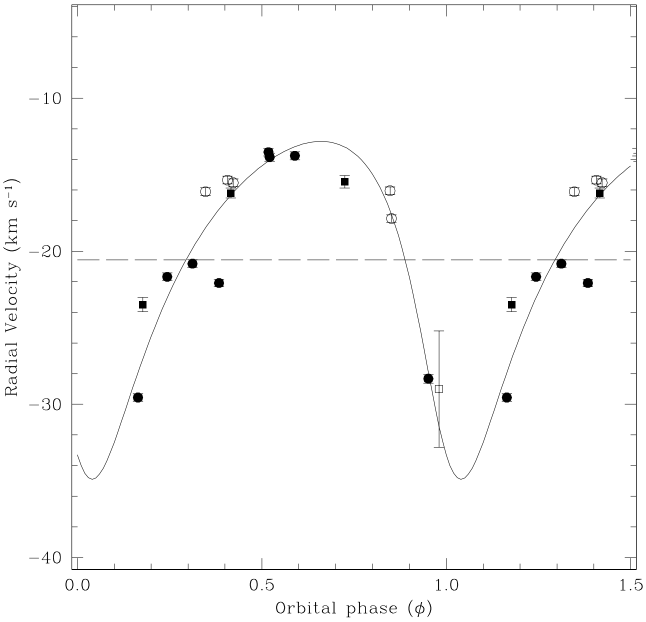

Fig. 5. Radial velocity curve for our target. The black dots represent RVs from FIES/NOT and the black squares ones from ESPADONS/CFHT. The error bars are as large as three σ. The literature value from Binks & Jeffries (2016) is plotted as an open square, and those from Jönsson et al. (2020) as open circles.

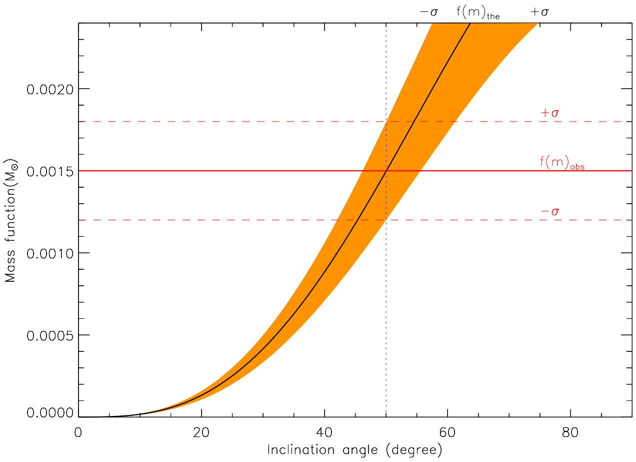

Fig. 6. Theoretical mass function vs the inclination angle. Horizontal red lines represent the mass function derived from the orbital solution. The vertical blue dotted line represents the inclination angle estimated for our star. The orange surface represents the ±1σ confidence level. The inclination angle of $i = 50°$ (see Sect. 4.1) implies a theoretical mass function computed with $M_2\ (\mathrm{M}_{\odot}) = 0.0245\,^{-0.0027}_{+0.0025}$.

By using all the velocities, orbital elements were determined by a weighted least-squares fitting to Eq. (1). Errors were estimated as the variation in the parameters that increases the χ^2 of a unity.

P: 13.976 ± 0.001 d
T: 2457532.966 ± 0.060
e: 0.35 ± 0.03
ω: 148° ± 2°
K: $11.0 \pm 0.5\ \mathrm{km\,s^{-1}}$
γ: $-\,20.5 \pm 0.2\ \mathrm{km\,s^{-1}}$
$a \sin i$: $2.8 \pm 0.2\ \mathrm{R}_{\odot}$
$f(m)$: $(1.6 \pm 0.3) \cdot 10^{-3}\ \mathrm{M}_{\odot}$

where the mass function, $f(m)$, is defined as

$$f(m) = \left(\frac{M_2}{M_1 + M_2}\right)^2 M_2 \sin^3 i. \tag{3}$$

This solution has been overplotted on the measured velocities in Fig. 5.

By using the previous solution, we have speculated about the mass of the companion under two hypotheses on the mass of the primary, which is fixed to $M_1 = 0.40\,\mathrm{M}_{\odot}$ (Drilling & Landolt 2000), and on the inclination angle of the orbit, $i = 50°$ (see Sect. 4.1). Solving Eq. (3) graphically, as is shown in Fig. 6, we obtained a value for the companion of $\mathrm{M}_2\ (\mathrm{M}_{\odot}) = 0.0245^{-0.0027}_{+0.0025}$. We note that since the orbital period, $P_{\mathrm{orb}} = 13.976$ d, is not supported, even if not disproven, by the periodogram analysis of the RV time series, we conservatively consider our orbital solution to be tentative.

6. Spot model

As will be discussed in Sect. 7, the observed photometric variability among different mechanisms may originate from surface brightness inhomogeneities of a magnetic nature. In this case, in order to investigate the surface distribution of brightness inhomogeneities (spots) on 2MASS J15594729+4403595 and their time evolution, we applied the spot modelling approach already introduced in Sect. 3 of Bonomo & Lanza (2012), to which we refer the reader for details. A brief summary is given in Appendix B. As a result of our modelling, we obtained a time series of maps of the spotted surface of 2MASS J15594729+4403595. The maps versus time of the spot distribution across the photosphere are plotted in Fig. 7. From left to right, the maps refer to the TESS Sectors 25, 50, and 51. In each sector, time series have been divided into two intervals to prevent the data gaps (see Fig. 3) from affecting the modelling.

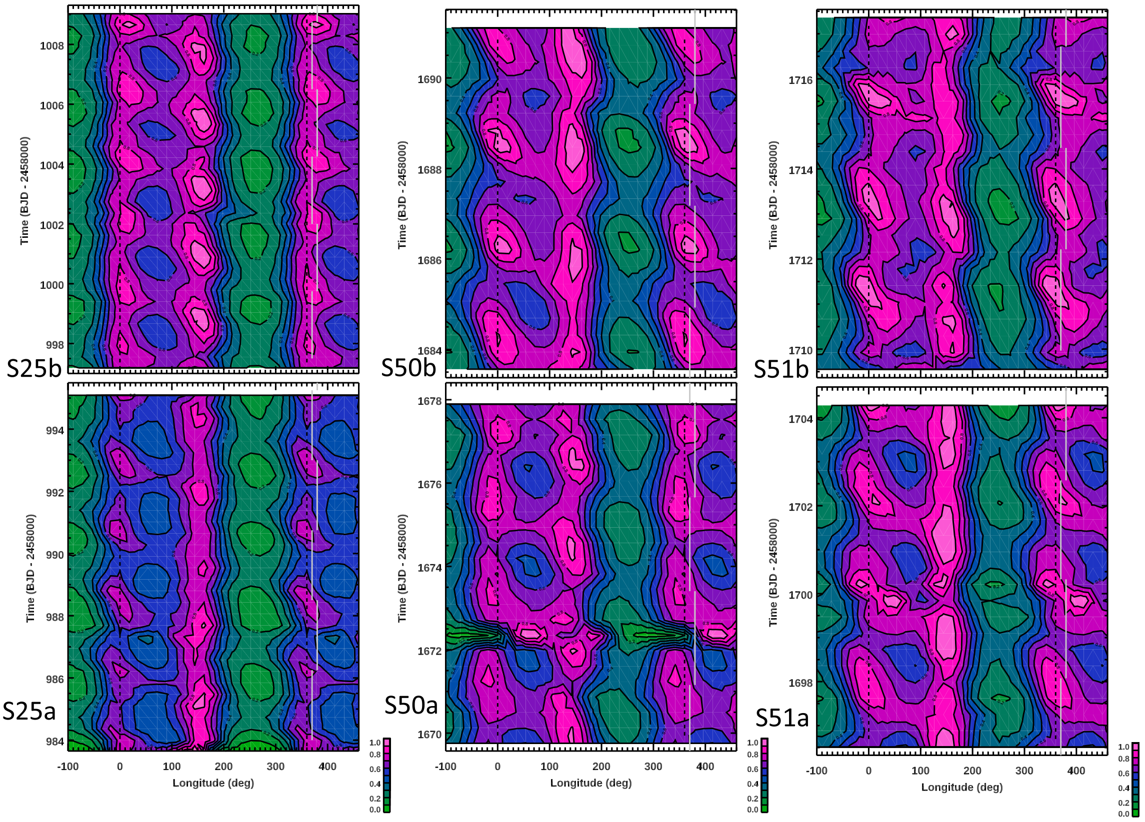

Fig. 7. Distribution of the spot filling factor vs the longitude and time derived by our maximum-entropy spot model of the TESS light curves in Sectors 20, 50, and 51. The maximum of the filling factor is indicated by the purple colour and the minimum by dark blue (see colour scale in the lower right corners). We note that the longitude scale is repeated beyond the [0°, 360°] interval to better follow the migration of the spot features. Each TESS sector is split into two intervals to skip the data gap. The solid white lines help one to track the spot evolution from one active longitude to the other.

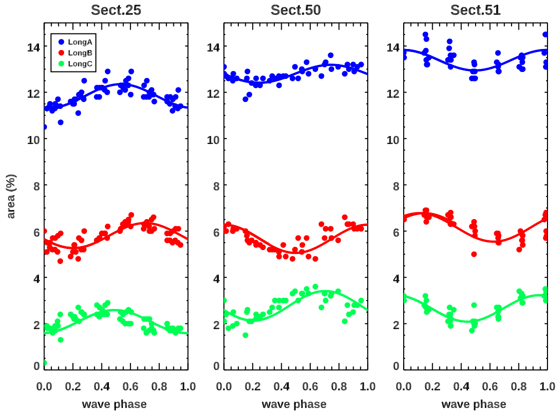

Fig. 8. Spot area at each active longitude vs the phase of the presumed Rieger cycle, whereby phases were computed using the area modulation period, P = 2.25 d. It is evident that spots A and B share the highest activity level, whereas spot C has marginal activity. The area modulation of spots A and B is in opposition, with activity at maximum in one longitude when at minimum in the opposite longitude.

We note that spot activity in our reference frame is permanently located at two longitudes centred at about 0° (hereafter, LongA) and 160° (hereafter, LongB), whereas a very marginal activity level is at 270° (hereafter LongC). We selected the origin of the longitudes so as to have the first active longitude at longitude zero at the beginning of our time series. On longitudes LongA and LongB, the level of spottedness evolves periodically with time, with a period of about 2.25 days, resulting from a periodogram analysis of their spotted area. However, the activity levels in the two longitudes are approximately in anti-phase; that is, when the activity is maximal at LongA, it is minimal at LongB and vice versa. Handmade vertical white lines help us to track the periodicity of 2.25 days. Therefore, we observe two brightness waves on opposite hemispheres that evolve in about six stellar rotations and that are in anti-phase.

The periodic spottedness change at each active longitude is more visible when the respective spot area is plotted versus its cycle phase, as in Fig. 8.

In principle, the retrieved spot pattern may be an artifact of the model, arising from the attempt of the spot code to reproduce the beat-like pattern of the observed light curve. To explore this possibility, we performed two tests. They consist of hypothesising two different causes for the observed variability (specifically, surface differential rotation (SDR) and Rieger cycles), generating synthetic light curves, and checking whether the maps are consistent with the hypothesised scenarios. Both tests are discussed in more detail in Appendix B. As a result, comparing our Tests 1 and 2 with the maps obtained from the observed data, we are confident that the maps we retrieved from real data are not an artifact but consistently reproduce a physical phenomenon.